


## Helicity-dependent optical control of the magnetization state emerging from the Landau-Lifshitz-Gilbert equation

Benjamin Assouline<sup>✉</sup> and Amir Capua<sup>✉\*</sup>

*Institute of Electrical Engineering and Applied Physics, The Hebrew University of Jerusalem, Jerusalem 9190401, Israel*

 (Received 19 January 2023; revised 18 May 2023; accepted 6 December 2023; published 3 January 2024)

It is well known that the Gilbert relaxation time of a magnetic moment scales inversely with the magnitude of the externally applied field,  $H$ , and the Gilbert damping,  $\alpha$ . Therefore, in ultrashort optical pulses, where  $H$  can temporarily reach high amplitudes, the Gilbert relaxation time can momentarily be extremely short, reaching even picosecond timescales. Here we show that for strong enough ultrashort pulses, the magnetization can respond within the optical cycle such that the optical control of the magnetization emerges by merely considering the optical magnetic field in the Landau-Lifshitz-Gilbert (LLG) equation. Surprisingly, when circularly polarized optical pulses are introduced, an optically induced helicity-dependent torque results. We find that the strength of the interaction is determined by  $\eta = \alpha\gamma H/f_{\text{opt}}$ , where  $f_{\text{opt}}$  and  $\gamma$  are the optical frequency and gyromagnetic ratio, respectively. Our results illustrate the generality of the LLG equation to the optical limit and the pivotal role of the Gilbert damping in the general interaction between optical magnetic fields and spins in solids.

DOI: [10.1103/PhysRevResearch.6.013012](https://doi.org/10.1103/PhysRevResearch.6.013012)

### I. INTRODUCTION

The ability to control the magnetization order parameter using ultrashort circularly polarized (CP) optical pulses has attracted a great deal of attention since the early experiments of the all-optical helicity dependent switching (AO-HDS) [1]. This interaction was found intriguing since it appears to have all the necessary ingredients to be explained by a coherent transfer of angular momentum, yet it occurs at photon energies of 1–2 eV, very far from the typical resonant transitions in metals. The technological applications and fundamental scientific aspects steered much debate and discussion, and the experiments that followed found dependencies on a variety of parameters including material composition [2–4], magnetic structure [5,6], and laser parameters [1,7,8], that were often experiment specific. Consequently, a multitude of mechanisms that entangle photons, spins, and phonons have been discovered [9].

Ferromagnetic resonance (FMR) experiments are usually carried out at the GHz range. In contrast, optical fields oscillate much faster, at  $\sim 400$ – $800$  THz. Therefore, it seems unlikely that such fast-oscillating fields may interact with magnetic moments. However, the amplitude of the magnetic field in ultrashort optical pulses can, temporarily, be very large such that the magnetization may respond extremely fast. For example, in typical experiments [1,7,10] having 40-fs–1-ps pulses at 800 nm, with energy of 0.5 mJ that are focused

to a spot size of  $\sim 0.5$  mm<sup>2</sup>, the peak magnetic flux density can be as high as  $\sim 5$  T, for which the corresponding Gilbert relaxation time reduces to tens of picoseconds in typical ferromagnets.

Here we show that ultrashort optical pulses may control the magnetization state by merely considering the optical magnetic field in the Landau-Lifshitz-Gilbert (LLG) equation. The principle behind the interaction is that the magnetization is incrementally affected within each optical cycle, such that a significant net torque can build up over the entire pulse duration in typical experimental conditions. We find that the strength of the interaction is determined by  $\eta = \alpha\gamma H/f_{\text{opt}}$ , where  $f_{\text{opt}}$  and  $\alpha$  are the angular optical frequency and the Gilbert damping, respectively, and  $\gamma$  is the gyromagnetic ratio. Accordingly, the loss of spin angular momentum to the lattice is key to the interaction. Moreover, we show that for circularly polarized pulses, the polarity of the optically induced torque is determined by the optical helicity. From a quantitative analysis, we find that a sizable effective out-of-plane field is generated, which is comparable to that measured experimentally in ferromagnet/heavy-metal (FM/HM) material systems [11]. However, our calculations indicate that an additional in-plane field is required to explain the experimental observations such as the optical spin-transfer torque (OSTT) [12] explored by Freimuth *et al.* [13]. Our results provide an additional torque to the AO-HDS [1,6,14–16] that has been considered on grounds of thermal [17–21], photomagnetic [22,23], and optomagnetic [7,11,24] mechanisms. The critical role of  $\alpha$  brings an additional explanation as to why a helicity-dependent torque is found in a variety of material systems that consist of heavy metals, such as Pt and Pd [6,13,25,26], which are excellent absorbers of spin angular momentum.

The LLG equation is typically not applied in the optical limit, and hence requires an alternative mathematical framework whose principles we adopt from the Bloch equations

\*amir.capua@mail.huji.ac.il

*Published by the American Physical Society under the terms of the Creative Commons Attribution 4.0 International license. Further distribution of this work must maintain attribution to the author(s) and the published article's title, journal citation, and DOI.*

for semiconductor lasers [27–29]. We exploit the analogy between the magnetization state and the Bloch vector of a two-level system (TLS) [30–34] by transforming the LLG equation under a time-varying magnetic field excitation to the dynamical Maxwell-Bloch equations in the presence of an electrical carrier injection. In this transformation, the  $+\hat{z}$  and  $-\hat{z}$  components of the magnetization are mapped to the occupation of the ground- and excited states of the TLS so that the reversal of the magnetization is described in terms of population transfer between the states.

The paper is organized as follows: We begin by transforming the LLG equation to the density matrix equations of a TLS. We then identify the mathematical form of a time-dependent magnetic field in the LLG equation,  $\vec{H}_{\text{pump}\downarrow\uparrow}$ , that is mapped to a time-independent carrier injection rate into the TLS. Such excitation induces a population transfer that varies linearly in time, and accordingly to a magnetization switching profile that is also linear in time. The mathematical  $\vec{H}_{\text{pump}\downarrow\uparrow}$  field emerges naturally as a temporal impulse-like excitation. We then show that when  $\alpha$  is sizable,  $\vec{H}_{\text{pump}\downarrow\uparrow}$  acquires a CP component whose handedness is determined by the direction of the switching. By substituting  $\vec{H}_{\text{pump}\downarrow\uparrow}$  for an experimentally realistic picosecond CP Gaussian optical magnetic pulse, we show that it can also exert a net torque on the magnetization. In this case as well, the helicity determines the polarity of the torque. Finally, we present a quantitative analysis that is based on experimental data [11].

## II. RESULTS

### A. Derivation of $\vec{H}_{\text{pump}\downarrow\uparrow}$

The LLG equation describing the dynamics of the magnetization,  $\vec{M}$ , where the losses are introduced in the Landau-Lifshitz form is given by [35]

$$\frac{d\vec{M}}{dt} = -\frac{\gamma}{1+\alpha^2}\vec{M} \times \vec{H} - \frac{\gamma\alpha}{1+\alpha^2}\frac{1}{M_s}\vec{M} \times \vec{M} \times \vec{H}. \quad (1)$$

Here  $M_s$  and  $\vec{H}$  are the magnetization saturation and the time-dependent externally applied magnetic field, respectively. We define  $\vec{H}_{\text{eff}}$  by

$$\vec{H}_{\text{eff}} \triangleq \left( \vec{H} - \frac{\alpha}{M_s} \vec{H} \times \vec{M} \right), \quad (2)$$

and in addition,  $\kappa \triangleq \frac{\gamma}{1+\alpha^2}(H_{\text{eff } x} - jH_{\text{eff } y})/2$  and  $\kappa_0 \triangleq \frac{\gamma}{1+\alpha^2}H_{\text{eff } z}$ , where  $\kappa$  and  $\kappa_0$  can be regarded as effective AC and DC magnetic fields acting on  $\vec{M}$ , respectively [31]. We transform  $\vec{M}$  to the density matrix elements of the Bloch state in the TLS picture having energy quantization along  $\hat{z}$  by substituting the longitudinal component of  $\vec{M}$  for the population difference,  $\rho_{11} - \rho_{22} = M_z/M_s$ , and the transverse components for the off-diagonal term  $\rho_{12} = (M_x - jM_y)/2M_s$  [36]. The normalization condition is  $\rho_{11} + \rho_{22} = M_s$ . Under this transformation, the LLG equation takes the form

$$\begin{aligned} \dot{\rho}_{11} &= -j\kappa\rho_{21} + \text{c.c.} \\ \dot{\rho}_{22} &= j\kappa\rho_{21} + \text{c.c.} \\ \dot{\rho}_{12} &= -j\kappa_0\rho_{12} + j\kappa(\rho_{11} - \rho_{22}). \end{aligned} \quad (3)$$

Equation (3) describes a general TLS subjected to an effective field via  $\kappa$  and  $\kappa_0$ . We compare it to the Bloch equations

describing a semiconductor laser that is electrically pumped [28,36,37]:

$$\begin{aligned} \dot{\rho}'_{11} &= \Lambda_1 - \gamma_1\rho_{11} + \frac{j}{2}[(\rho_{12} - \rho_{21})(V_{12} + V_{21}) \\ &\quad - (\rho_{12} + \rho_{21})(V_{12} - V_{21})] \\ \dot{\rho}'_{22} &= \Lambda_2 - \gamma_2\rho_{22} - \frac{j}{2}[(\rho_{12} - \rho_{21})(V_{12} + V_{21}) \\ &\quad - (\rho_{12} + \rho_{21})(V_{12} - V_{21})] \\ \dot{\rho}'_{12} &= -(j\omega_{\text{TLS}} + \gamma_{\text{inh}})\rho_{12} + j(\rho_{11} - \rho_{22})V_{12}. \end{aligned} \quad (4)$$

In this reference model,  $\Lambda_1$  and  $\Lambda_2$  are injection rates of carriers to the ground and excited states of the TLS, respectively. They are assumed to be time independent and represent a constant injection of carriers from an undepleted reservoir [28].  $\gamma_1$  and  $\gamma_2$  are the relaxation rates of the ground and excited states, and  $\gamma_{\text{inh}}$  is the decoherence rate due to an inhomogeneous broadening.  $V_{12}$  is the interaction term and  $\omega_{\text{TLS}}$  is the resonance frequency of the TLS. Typically,  $\hbar\omega_{\text{TLS}}$  represents a time-independent interband energy gap, where  $\hbar$  is the reduced Planck constant. However, here  $\omega_{\text{TLS}}$  can depend on time. Figure 1(a) illustrates schematically the analogy between the magnetization dynamics and the electrically pumped TLS. From Eqs. (3) and (4) we find the connection between the LLG equation expressed in the density matrix form and the model of the electrically pumped TLS:

$$\begin{aligned} \Lambda_1 - \gamma_1\rho_{11} + [M_y\Re\{V_{12}\} + M_x\Im\{V_{12}\}] &= -j\kappa\rho_{21} + \text{c.c.} \\ \Lambda_2 - \gamma_2\rho_{22} - [M_y\Re\{V_{12}\} + M_x\Im\{V_{12}\}] &= j\kappa\rho_{21} + \text{c.c.} \\ -(j\omega_{\text{TLS}} + \gamma_{\text{inh}})\rho_{12} + jM_zV_{12} &= -j\kappa_0\rho_{12} + j\kappa M_z. \end{aligned} \quad (5)$$

The pumping of the excited and ground states by the constant  $\Lambda_1$  and  $\Lambda_2$  rates implies that the reversal of the magnetization along the  $\mp\hat{z}$  direction is linear in time. Using Eq. (5) we find  $\kappa$ , and hence a field  $\vec{H}$ , that produces such  $\Lambda_1$  and  $\Lambda_2$ . The application of such a field as the sole excitation in the LLG equation results in  $\gamma_1 = \gamma_2 = V_{12} = 0$ , and consequently  $\rho'_{11} = \Lambda_1 = -\Lambda_2$ . We define this field as  $\vec{H}_{\text{pump}\downarrow\uparrow}$ :

$$\vec{H}_{\text{pump}\downarrow\uparrow} = \frac{\pm\Lambda_p}{M_s^2 - M_z^2} \begin{pmatrix} M_y \\ -M_x \\ 0 \end{pmatrix}. \quad (6)$$

$\vec{H}_{\text{pump}\downarrow\uparrow}$  depends on the temporal state of  $\vec{M}$ , while  $\Lambda_p = \gamma\Lambda_1/(1+\alpha^2)$  is the effective field strength parameter. Applying such  $\vec{H}_{\text{pump}\downarrow\uparrow}$  requires to know *a priori* the state of  $\vec{M}$ ; therefore, we refer to it as a mathematical field.  $\vec{H}_{\text{pump}\downarrow}$  and  $\vec{H}_{\text{pump}\uparrow}$  induce a linear transition of  $\vec{M}$  towards the  $-\hat{z}$  and  $+\hat{z}$  direction, respectively. The constant carrier injection rate in the Bloch picture requires that  $\vec{H}_{\text{pump}\downarrow\uparrow}$  diverges as  $\vec{M}$  reaches the poles of the Bloch sphere.

Figure 1(b) presents the outcome of the application of  $\vec{H}_{\text{pump}\downarrow\uparrow}$  by numerically integrating the LLG equation.  $\vec{M}$  was initialized in the  $\hat{x}$  direction, so that  $\vec{H}_{\text{pump}\downarrow\uparrow}$  is polarized in the  $\hat{y}$  direction and drives  $\vec{M}$  in the  $\hat{z}$  direction. The figure illustrates  $\vec{H}(t)$ ,  $M_z(t)$ , and the  $\hat{z}$  torque,  $(-\vec{M} \times \vec{H})_z$ , for alternating  $\vec{H}_{\text{pump}\downarrow}$  and  $\vec{H}_{\text{pump}\uparrow}$  that switch  $\vec{M}$  between  $\mp M_s\hat{z}$ .

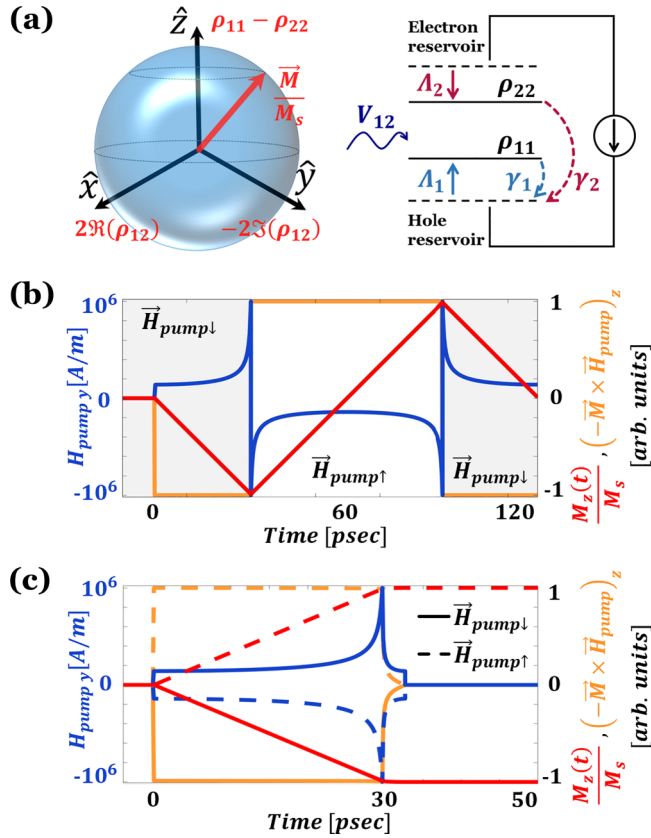


FIG. 1. (a) Left panel: Illustration of  $\vec{M}$  on the Bloch sphere. Right panel: Illustration of the electrically pumped TLS. (b) Interaction with  $\vec{H}_{\text{pump}\downarrow/\uparrow}$  of Eq. (6). The figure illustrates the temporal plots of  $M_z/M_s$ ,  $\vec{H}_{\text{pump}\downarrow/\uparrow}$ , and  $(-\vec{M} \times \vec{H})_z$  normalized to unity.  $|\Lambda_p| = 4.53 \times 10^{10} \text{ A}^2/\text{m}^2$ , corresponding to  $\Delta\tau_{\downarrow/\uparrow} = 30 \text{ ps}$ . Alternation between  $\vec{H}_{\text{pump}\downarrow}$  and  $\vec{H}_{\text{pump}\uparrow}$  is indicated by the shaded areas and occurs when  $|M_z|$  reaches  $0.99M_s$ . (c) Interaction with  $\vec{H}_{\text{pump}\downarrow/\uparrow}$  and a more realistic trailing edge, for the same conditions in (b). Full lines correspond to  $\vec{H}_{\text{pump}\downarrow}$  and dashed lines correspond to  $\vec{H}_{\text{pump}\uparrow}$ . The simulations in (b) and (c) are presented for  $M_s = 3 \times 10^5 \text{ A/m}$  and  $\alpha = 0.025$  [38], and  $\vec{H}_{\text{pump}\downarrow}$  was turned on at  $t = 0$ .

The magnitude of  $\Lambda_p$  determines the switching time,  $\Delta\tau_{\downarrow/\uparrow}$ , chosen here to describe a picosecond regime. Equation (5) yields  $\Delta\tau_{\downarrow/\uparrow} = (1 + \alpha^2)M_s/(\gamma\Lambda_p) \approx M_s/\gamma\Lambda_p$ , in which  $M_z$  is driven from  $M_z = 0$  to  $M_z \cong \pm M_s$  (for derivation, see Appendix A). It is seen that  $(-\vec{M} \times \vec{H})_z$  is constant when  $\vec{H}_{\text{pump}\downarrow}$  or  $\vec{H}_{\text{pump}\uparrow}$  are applied so that the switching profile of  $M_z$  is linear in time. It is also seen that  $\vec{H}_{\text{pump}\downarrow/\uparrow}$  requires that  $|\vec{H}|$  diverge as  $M_z$  approaches  $\pm M_s$ , which is not experimentally feasible. To account for a more realistic excitation, in Fig. 1(c) we simulated a pulse whose trailing edge was taken as a reflection in time of  $\vec{H}_{\text{pump}\downarrow/\uparrow}$ , and that is shorter by an order of magnitude as compared to the leading edge. In this case  $\vec{H} \neq \vec{H}_{\text{pump}\downarrow/\uparrow}$  and does not induce a transition so that  $\vec{M}$  remains in its final state when  $\vec{H}$  is eventually turned off.

### B. Effect of the Gilbert damping on $\vec{H}_{\text{pump}\downarrow/\uparrow}$

The polarization state of  $\vec{H}_{\text{pump}\downarrow/\uparrow}$  is determined from the polarization state of the transverse components of  $\vec{M}$ .

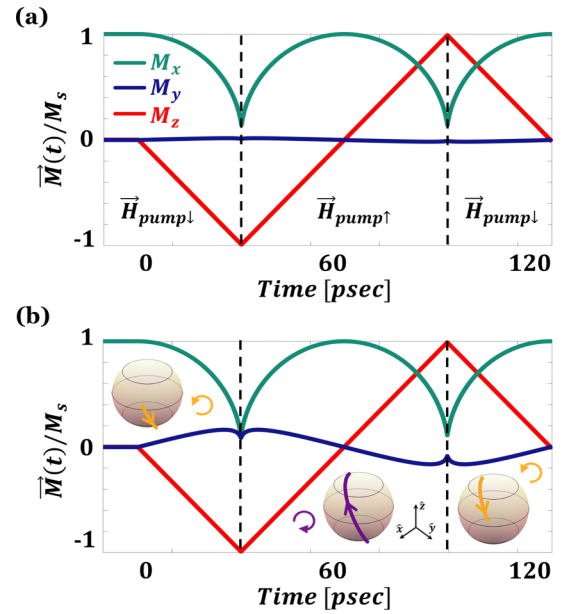


FIG. 2. Temporal evolution of the components of  $\vec{M}$  under the influence of alternating  $\vec{H}_{\text{pump}\downarrow}$  and  $\vec{H}_{\text{pump}\uparrow}$  for (a)  $\alpha = 0.025$  and (b)  $\alpha = 0.25$ . An RCP (LCP) component in the trajectory of  $\vec{M}$  is acquired for the application of  $\vec{H}_{\text{pump}\downarrow}$  ( $\vec{H}_{\text{pump}\uparrow}$ ). Insets illustrate the trajectory of  $\vec{M}$  along the Bloch sphere. Black dashed lines indicate the alternation between  $\vec{H}_{\text{pump}\downarrow}$  and  $\vec{H}_{\text{pump}\uparrow}$ . In panel (b)  $|\Lambda_p| = 4.78 \times 10^{10} \text{ A}^2/\text{m}^2$  to preserve  $\Delta\tau_{\downarrow/\uparrow}$  while the large  $\alpha$  was chosen for visualization purpose.

Particularly, if  $M_x(t)$  and  $M_y(t)$  follow a circular trajectory,  $\vec{H}_{\text{pump}\downarrow/\uparrow}$  acquires a CP component as readily seen from Eq. (6). In Figs. 1(b) and 1(c),  $\alpha$  was relatively small, so that the damping torque was negligible and  $\vec{M}$  remained in the  $x$ - $z$  plane. Therefore,  $\vec{H}_{\text{pump}\downarrow/\uparrow}$  remained linearly polarized in  $\hat{y}$ . Next, we show that for larger  $\alpha$ ,  $M_y(t)$  becomes appreciable such that  $\vec{H}_{\text{pump}\downarrow/\uparrow}$  acquires an additional CP component. This result emerges naturally from the Bloch picture: we recall that the transverse components of  $\vec{M}$  are expressed by the off-diagonal density matrix element,  $\rho_{12} = (M_x - jM_y)/2M_s$ . According to Eq. (4),  $\rho_{12}$  oscillates at  $\omega_{\text{TLS}}$  and decays at the rate  $\gamma_{\text{inh}}$ , whereas the sign of  $\omega_{\text{TLS}}$  determines the handedness of the transverse components of  $\vec{M}$ . Namely, the ratio between  $\omega_{\text{TLS}}$  and  $\gamma_{\text{inh}}$  determines the magnitude of the circular component in the  $(M_x(t), M_y(t))$  trajectory. Under the application of  $\vec{H}_{\text{pump}\downarrow/\uparrow}$ , Eq. (5) yields  $\omega_{\text{TLS}} = \pm\gamma\Lambda_p\alpha M_s/[(M_s^2 - M_z^2)(1 + \alpha^2)]$  and  $\gamma_{\text{inh}} = \mp\gamma\Lambda_p M_z/[(M_s^2 - M_z^2)(1 + \alpha^2)]$  readily showing that  $|\omega_{\text{TLS}}/\gamma_{\text{inh}}| = \alpha M_s/M_z$  increases with  $\alpha$ , so that  $\vec{H}_{\text{pump}\downarrow/\uparrow}$  acquires an additional CP component (see Appendix B for full derivation). Figure 2 illustrates these results. Panel (a) presents the components of  $\vec{M}(t)$  for the same simulation in Fig. 1(b). It is seen that  $M_y(t)$  is negligible and thus  $\vec{H}_{\text{pump}\downarrow/\uparrow}$  remains linearly polarized. When  $\alpha$  is increased, an elliptical trajectory of  $\vec{M}$  in the  $x$ - $y$  plane emerges, while the constant transition rate of  $M_z$  persists as illustrated in Fig. 2(b). In this case,  $\vec{H}_{\text{pump}\downarrow/\uparrow}$  acquires a right-CP (RCP) or left-CP (LCP) component depending on the choice of  $\vec{H}_{\text{pump}\downarrow}$  or  $\vec{H}_{\text{pump}\uparrow}$ .

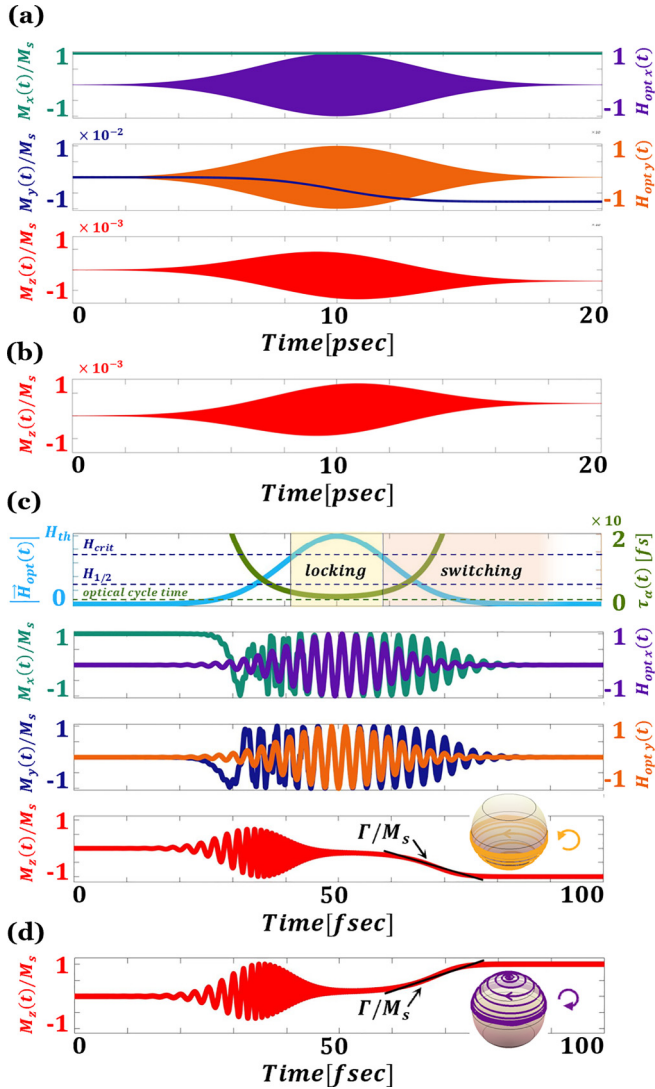


FIG. 3. (a) Magnetization reversal induced by an RCP Gaussian pulse for  $\alpha = 0.035$ ,  $M_s = 3 \times 10^5 \frac{\text{A}}{\text{m}}$ ,  $\eta = 2.5 \times 10^{-4}$ , and  $t_{\text{peak}} = 10$  ps. Top and middle panels depict the temporal evolution of the  $x$  and  $y$  components of  $\vec{M}$  and  $\vec{H}_{\text{opt}}$  in normalized units. Bottom panel depicts  $M_z/M_s$ . (b)  $M_z/M_s$ , for the application of an LCP pulse. (c) Magnetization reversal induced by an RCP Gaussian pulse for  $\eta = 1$  and  $t_{\text{peak}} = 50$  fs. Top panel presents the temporal behavior of  $|\vec{H}_{\text{opt}}|$  and  $\tau_\alpha$ , where  $H_{\text{crit}} = H_{\text{th}}/\sqrt{2}$  and  $H_{1/2} = 0.27H_{\text{th}}$ . Second and third panels depict the temporal evolution of the  $x$  and  $y$  components of  $\vec{M}$  and  $\vec{H}_{\text{opt}}$  in normalized units. Bottom panel depicts  $M_z/M_s$ . (d)  $M_z/M_s$ , for the application of an LCP pulse. In (c) and (d), black solid lines represent the analytical solution of  $\Gamma/M_s$ . Insets: trajectory along the Bloch sphere for  $t > 55$  fs.

### C. Interaction with optical CP Gaussian pulses

The coupling between the handedness and reversal direction in an ultrashort excitation is reminiscent of the switching reported in AO-HDS experiments [1,7,8,18] and emerges naturally in our model. These results call to examine the interaction of the CP magnetic field of a short optical pulse with  $\vec{M}$ . Figure 3(a) presents the calculation for experimentally realistic settings following Refs. [7,10,18], where only the optical magnetic field is substituted into the LLG

equation. The results are shown for an 800-nm optical magnetic field of an RCP Gaussian optical pulse modeled by  $\vec{H}_{\text{opt}}(t) = H_{\text{peak}} \frac{\cos(\omega_{\text{opt}} t)}{\sin(\omega_{\text{opt}} t)} e^{-(t-t_{\text{peak}})^2/2\tau_p^2}$ . The pulse has a duration determined by  $\tau_p$ , an angular frequency  $\omega_{\text{opt}}$ , and a peak amplitude  $H_{\text{peak}}$  that is reached at  $t = t_{\text{peak}}$ . In our simulations  $\tau_p = 3$  ps and  $t_{\text{peak}} = 10$  ps. The pulse energy was  $\sim 5$   $\mu\text{J}$  and assumed to be focused to a spot size of  $\sim 100$   $\mu\text{m}^2$ , for which  $H_{\text{peak}} = 8 \times 10^6$  A/m. Such spot size is much larger than typical size of a domain wall; therefore, the exchange energy is accounted for in the macrospin approximation. Here we take  $\alpha = 0.035$ , which is typical for Pt/Co-based systems [6,13,25,39]. For such conditions, the Gilbert relaxation time corresponding to  $H_{\text{peak}}$  is  $\tau_\alpha = \frac{1}{\alpha\gamma H_{\text{peak}}} \approx 16$  ps [40,41]. It is readily seen that for such  $\tau_\alpha$  the magnetization responds within the duration of the optical pulse, indicating that the interaction between the optical pulse and  $\vec{M}$  becomes possible by the LLG equation. Following the interaction,  $M_z = -5 \times 10^{-4} \cdot M_s$ , namely a sizable net longitudinal torque results, which builds up from cycle to cycle of the optical radiation. This torque is not affected significantly by the anisotropy field, as discussed in Appendix C.

This mechanism is fundamentally different from the precessional switching mechanism by an optically induced DC longitudinal field. Such field can be generated, for example, by the inverse Faraday effect (IFE), which arises from the optical electrical field in contrast to the optical magnetic field considered here. An equivalent effective DC magnetic field,  $B_{\text{eff}}^z$ , required for such transition within 10 ps is estimated to be  $\sim 50$  mT (see Appendix C). In agreement with the prediction of the TLS model, pulses of the opposite helicity induce an opposite transition as shown in Fig. 3(b). The strength of the interaction depends on the ability of  $\vec{M}$  to decay towards the oscillating optical magnetic field within the optical cycle. Hence, the magnitude of  $\tau_\alpha$  is key to the interaction. Accordingly, for a given pulse duration, we define the interaction strength parameter  $\eta = 2\pi\alpha\gamma H_{\text{peak}}/\omega_{\text{opt}}$ , which expresses the ratio between  $\tau_\alpha$  and the optical cycle and is  $2.5 \times 10^{-4}$  in Fig. 3(a).

### D. Dynamics in the $\eta \rightarrow 1$ limit

The principles of the interaction can be better understood at the limit where  $\eta \rightarrow 1$  and for which the interaction can be described analytically. To this end, we set  $\eta = 1$  so that the Gilbert relaxation time equals the optical cycle. The higher optical magnetic fields required for this limit are achievable using conventional amplified femtosecond lasers, for example by focusing an  $\sim 5$ -mJ pulse into a spot size of  $\sim 1$   $\mu\text{m}^2$ . However, in practical experiments such pulses surpass the typical damage threshold of the metallic film. Nevertheless, the study of the LLG equation in this limit is instructive. Figure 3(c) illustrates the results for an RCP  $\vec{H}_{\text{opt}}$  pulse of a duration of 20 fs determined by the full width at half maximum of the intensity. The figure reveals the different stages of the interaction. During the leading edge, for  $t < \sim 40$  fs, the relative phase between  $\vec{H}_{\text{opt}}$  and  $\vec{M}$  seems arbitrary. As  $t_{\text{peak}}$  is reached, the Gilbert relaxation time becomes as short as the optical cycle, allowing  $\vec{M}$  to follow  $\vec{H}_{\text{opt}}$  until it is entirely locked to  $\vec{H}_{\text{opt}}$ . In this case,  $\vec{M}$  undergoes a right-circular trajectory

about  $\hat{z}$ . The switching of  $\vec{M}$  takes place at the final stage of the interaction: During the trailing edge of the pulse, the amplitude of  $\vec{H}_{\text{opt}}$  reduces and  $\tau_\alpha$  extends, thereby releasing the locking between  $\vec{M}$  and  $\vec{H}_{\text{opt}}$ . In this case, the switching profile of  $M_z$  is monotonic linear-like in time, closely resembling the transition stemming from a constant carrier injection rate in the Bloch picture. The optically induced transition can be described analytically following the calculation presented in Appendix D, from which we find the transition rate:

$$\Gamma/M_s = \mp \frac{3}{2\sqrt{2}} \ln\left(\frac{4}{3}\right) \frac{1}{\tau_p \left[ \sqrt{\ln\left(\frac{H_{\text{peak}}}{0.27H_{\text{th}}}\right)} - \sqrt{\ln\left(\frac{H_{\text{peak}}}{H_{\text{th}}/\sqrt{2}}\right)} \right]}, \quad (7)$$

where  $H_{\text{th}} = \frac{\omega_{\text{opt}}}{2\pi\gamma\alpha}$  is the value of  $H_{\text{peak}}$  at  $\eta = 1$ . The rate  $\Gamma/M_s$  is plotted as well in Fig. 3(c) and reproduces the numerical calculation.  $\Gamma$  depends on the ratio between  $H_{\text{peak}}$  and  $H_{\text{th}}$  and is only weakly dependent on  $H_{\text{peak}}$ . Namely, when  $H_{\text{peak}} \gg H_{\text{th}}$ , the circular trajectory of  $\vec{M}$  in the  $x$ - $y$  plane persists longer after  $t_{\text{peak}}$ , but as the amplitude of the pulse decays below  $H_{\text{th}}/\sqrt{2}$ ,  $\vec{M}$  is driven out of the  $x$ - $y$  plane and the reversal takes place (see Appendix E). This analysis also holds for LCP pulses, which result in an opposite reversal of  $\vec{M}$ , as shown in Fig. 3(d).

### III. DISCUSSION: COMPARISON WITH EXPERIMENTS

$\eta$  describes the efficiency of the interaction, namely, the ability of  $\vec{M}$  to follow  $\vec{H}_{\text{opt}}$ . When  $\eta \ll 1$ , as in the case of experimentally realistic intensities, the transition is partial as seen in Figs. 3(a) and 3(b). In this case, an incremental torque acts on the magnetization within each optical cycle and builds up to a sizable effective torque over the pulse duration. This illustrates the pivotal role of  $\alpha$  since  $\eta \propto \alpha$ , and is explored in detail in Appendix E. Interestingly, the AO-HDS effect was found in a variety of material systems that included Pt, which was introduced to induce a perpendicular magnetic anisotropy [25,26] by the Pt/Co interface. However, Pt is also well known to be an efficient sink for spin angular momentum [42,43]; therefore, it also increases  $\alpha$  and enhances the optically induced torque according to the LLG equation. This trend is readily seen in the measurements carried out by Choi *et al.* [11] in a variety of FM/HM systems.

The time-resolved magnetization dynamics measured in Ref. [11] further provide quantitative data for testing our calculations. To this end, we simulate an optical pulse having a fluence of  $2.35 \text{ mJ/cm}^2$  and the same sample parameters of the Co/Pt and Fe/Pt systems of Ref. [11] (Appendix C). From the response of  $M_y$ , Choi *et al.* estimated  $B_{\text{eff}}^z = 1 \text{ mT}$ . Following the same analysis, we find from our calculations  $B_{\text{eff}}^z = 0.25 \text{ mT}$ , which is of the same order of magnitude. Choi *et al.* further calculated  $B_{\text{eff}}^z$  induced by the IFE from the theories by Mondal [44], Berrita [45], and Qaiumzadeh [46], and found a large range of predicted  $B_{\text{eff}}^z \sim 3 \times 10^{-6} - 40 \text{ T}$  for the same conditions. Additionally, from the theory derived by Freimuth *et al.* [13] that was based on first-principles electronic structure calculations and the Keldysh nonequilibrium formalism, Choi

*et al.* estimated  $B_{\text{eff}}^z \sim 1.5 - 20 \text{ mT}$ . Overall, it is seen that the effective transverse torque emerging from the LLG equation can be of comparable magnitude to that generated by the IFE.

In the same manner, an effective transverse field  $B_{\text{eff}}^y$  can also be evaluated from the  $M_z$  dynamics. From the experimental data presented by Choi *et al.*,  $B_{\text{eff}}^y$  is found to be in the range of  $\sim 0.05 - 0.87 \text{ mT}$  for the various Co-, Fe-, and Ni-based samples. In our calculations we find  $B_{\text{eff}}^y = 0.014 \text{ mT}$ . Namely, an additional contribution to  $B_{\text{eff}}^y$  should be accounted for. Freimuth *et al.* [13] found that the electrical field associated with the magnetic field of the typical ultrashort pulses affects the electronic band structure. Consequently, the resultant nonequilibrium Keldysh states were shown to induce an OSTT [12] wherein spin-polarized photocarriers are generated according to the optical selection rules and contribute to  $B_{\text{eff}}^y$ . Namely, the helicity-dependent torque stemming from our calculations should be considered alongside the IFE and OSTT mechanisms. Interestingly, Freimuth *et al.* [13] showed that the IFE and OSTT mechanisms are enhanced by the spin-orbit coupling (SOC). Considering the LLG equation, SOC also enhances  $\alpha$  and consequently also the efficiency parameter  $\eta$ , resulting in a larger optically induced torque.

### IV. SUMMARY

To summarize, in this work we demonstrated that the control of the magnetization by an optical field arises from first principles by introducing the magnetic part of the optical radiation to the LLG equation. The principle of the interaction is that the magnetization is incrementally affected within each optical cycle such that a significant net torque can build up over the entire pulse duration. This was seen from the comparison between the experimentally realistic case where  $\eta \ll 1$  and the case of  $\eta = 1$ . The process is independent of resonance conditions and is enhanced with increasing magnetic field amplitude and Gilbert damping. Using the TLS model, we demonstrated the coupling between the optical helicity state and the polarity of the longitudinal torque. A quantitative analysis of the optically induced torque revealed that it can be comparable to that generated by the IFE, and further stressed the important role of the OSTT. Our results illustrate the generality of the LLG equation to the optical limit in the interaction between optical magnetic fields and spins in solids.

### ACKNOWLEDGMENTS

A.C. and B.A. acknowledge the support from the Israel Science Foundation (Grant No. 1217/21), the Peter Brojde Center for Innovative Engineering and Computer Science, and from the Center for Nanoscience and Nanotechnology of the Hebrew University of Jerusalem.

### APPENDIX A: MAGNETIZATION SWITCHING USING $\vec{H}_{\text{pump}}$

We start with the calculation of the time duration  $\Delta\tau$  during which the  $\vec{H}_{\text{pump}\downarrow\uparrow}$  fields have to be applied in order to reverse the magnetization state, i.e., to drive  $M_z$  from  $M_z = 0$  to  $M_z = M_s$  (in the main text,  $\vec{M}$  is initialized in the  $\hat{x}$

direction). Assuming that  $\vec{H}_{\text{pump}\downarrow\uparrow}$  is the sole excitation acting on  $\vec{M}$ , we have

$$|\dot{M}_z| = |\rho_{11} - \rho_{22}| = |\Lambda_1 - \Lambda_2|. \quad (\text{A1})$$

Under the application of  $\vec{H}_{\text{pump}\downarrow\uparrow}$ ,  $\Lambda_1 = -\Lambda_2$ , so that

$$|\dot{M}_z| = 2|\Lambda_1|. \quad (\text{A2})$$

We integrate both sides, for the duration  $\Delta\tau$  during which  $M_z$  increases from 0 to  $M_s$ :

$$\int_0^{\Delta\tau} 2\Lambda_1 = \int_0^{\Delta\tau} M_z. \quad (\text{A3})$$

The right-hand-side is simply multiplied by  $\Delta\tau$ , as  $\Lambda_1$  is a constant:

$$2\Lambda_1\Delta\tau = M_s. \quad (\text{A4})$$

We express  $\Lambda_1$  using  $\Lambda_p$ :

$$\frac{\gamma\Lambda_p}{(1+\alpha^2)}\Delta\tau = M_s. \quad (\text{A5})$$

Finally,

$$\Delta\tau = \frac{(1+\alpha^2)}{\gamma\Lambda_p}M_s. \quad (\text{A6})$$

### Parameters

The parameters of the simulations of Figs. 1 and 2 in the main text were chosen to model a realistic NM-FM bilayer sample such as the Pt/CoFeB system [47] with  $\alpha = 0.025$ , thickness of the FM layer of  $t_{\text{FM}} = 12 \text{ \AA}$ , and saturation magnetization of  $M_s = 3 \times 10^5 \text{ A/m}$ . In Fig. 3 in the main text,  $\alpha = 0.035$ , which is typical for Pt/Co-based systems [39,48]

## APPENDIX B: CALCULATION OF THE TLS TERMS

We implement the procedure described in Eq. (5) in the main text in order to derive expression for the TLS terms  $\Lambda_1$ ,  $\Lambda_2$ ,  $\gamma_1$ ,  $\gamma_2$ ,  $\gamma_{\text{inh}}$ ,  $\omega_{\text{TLS}}$ , and  $V_{12}$  as a function of terms from the LLGS equation  $\vec{M}$ ,  $\alpha$ , and  $\Lambda_p$ . The field  $\vec{H}_{\text{pump}\downarrow\uparrow}$  from Eq. (6) in the main text has the following form:

$$\vec{H}_{\text{pump}\downarrow\uparrow} = \frac{\pm\Lambda_p}{M_s^2 - M_z^2} \begin{pmatrix} M_y \\ -M_x \\ 0 \end{pmatrix}. \quad (\text{B1})$$

The “ $\pm$ ”-sign notation throughout this appendix corresponds to the application of either  $\vec{H}_{\text{pump}\downarrow}$  or  $\vec{H}_{\text{pump}\uparrow}$ , respectively.

We start with the generalized  $\vec{H}_{\text{eff}}$  field [Eq. (2) in the main text]:

$$\vec{H}_{\text{eff}} \equiv \left[ \vec{H} - \frac{\alpha}{M_s} \vec{H} \times \vec{M} \right]. \quad (\text{B2})$$

In component form it takes the following form:

$$\begin{aligned} \vec{H}_{\text{eff}} &= \begin{pmatrix} H_{\text{eff } x} \\ H_{\text{eff } y} \\ H_{\text{eff } z} \end{pmatrix} \\ &= \frac{\gamma}{1+\alpha^2} \begin{pmatrix} \mp\Lambda_p \frac{M_y}{M_s^2 - M_z^2} \mp \frac{1}{M_s} [\alpha\Lambda_p \frac{M_x}{M_s^2 - M_z^2} M_z] \\ \pm\Lambda_p \frac{M_x}{M_s^2 - M_z^2} \mp \frac{1}{M_s} [\alpha\Lambda_p \frac{M_y}{M_s^2 - M_z^2} M_z] \\ \pm \frac{\alpha}{M_s} \Lambda_p \end{pmatrix}. \end{aligned} \quad (\text{B3})$$

Next, we calculate  $\kappa$  and  $\kappa_0$  similarly to the main text:

$$\begin{aligned} \kappa &= \frac{\gamma}{2(1+\alpha^2)} (H_{\text{eff } x} - jH_{\text{eff } y}) \\ &= \mp j \frac{\gamma}{2(1+\alpha^2)} \Lambda_p \frac{M_x - jM_y}{M_s^2 - M_z^2}, \end{aligned} \quad (\text{B4})$$

$$\kappa_0 = B'_z = \pm \frac{\gamma}{1+\alpha^2} \frac{\alpha}{M_s} \Lambda_p. \quad (\text{B5})$$

Before starting the calculations, we point out a useful identity:

$$\begin{aligned} (M_x - jM_y)(M_x + jM_y) &= M_x^2 + M_y^2 = M_s^2 - M_z^2 \equiv 4\rho_{12}\rho_{21} \\ &= 4A_1A_2^*A_2A_1^* = 4|A_1|^2|A_2|^2 \\ &= 4\rho_{11}\rho_{22} = 4\rho_{11} \left( \frac{M_s - M_z}{2} \right) \\ &= 4\rho_{22} \left( \frac{M_s + M_z}{2} \right). \end{aligned} \quad (\text{B6})$$

We now start the calculation in order to express the TLS terms  $\Lambda_1$  and  $\Lambda_2$  from the rate equation of  $\rho_{11}$  [Eq. (3) in the main text]:

$$\dot{\rho}_{11} = j(\kappa^*\rho_{12} - \kappa\rho_{21}) = -j\rho_{21}\kappa + \text{c.c.} \quad (\text{B7})$$

Substituting  $\kappa$  from Eq. (B4):

$$\dot{\rho}_{11} = \frac{\gamma}{2(1+\alpha^2)} \frac{M_x + jM_y}{2} \left\{ \mp\Lambda_p \frac{M_x - jM_y}{M_s^2 - M_z^2} \right\} + \text{c.c.} \quad (\text{B8})$$

Using the identity from Eq. (B6):

$$\dot{\rho}_{11} = \mp \frac{\gamma}{2(1+\alpha^2)} \Lambda_p. \quad (\text{B9})$$

Similarly, for  $\rho_{22}$ :

$$\dot{\rho}_{22} = \pm \frac{\gamma}{2(1+\alpha^2)} \Lambda_p. \quad (\text{B10})$$

Using Eq. (4) in the main text:

$$\rho_{11} = \Lambda_1 - \gamma_1\rho_{11} + [M_y\Re\{V_{12}\} + M_x\Im\{V_{12}\}],$$

$$\rho_{22} = \Lambda_2 - \gamma_2\rho_{22} - [M_y\Re\{V_{12}\} + M_x\Im\{V_{12}\}].$$

Consequently, we express the TLS terms  $\Lambda_1$ ,  $\Lambda_2$ ,  $\gamma_1$ ,  $\gamma_2$ ,  $V_{12}$ :

$$\Lambda_1 = \mp \frac{\gamma}{2(1+\alpha^2)} \Lambda_p, \quad \Lambda_2 = \pm \frac{\gamma}{2(1+\alpha^2)} \Lambda_p,$$

$$\gamma_1 = 0, \quad \gamma_2 = 0, \quad V_{12} = 0.$$

Next, we express the two remaining TLS terms  $\omega_{\text{TLS}}$  and  $\gamma_{\text{inh}}$  using the rate equation of  $\rho_{12}$  in Eq. (3) the main text:

$$\dot{\rho}_{12} = -j\kappa_0\rho_{12} + j\kappa(\rho_{11} - \rho_{22}). \quad (\text{B11})$$

Substituting  $\kappa$  and  $\kappa_0$  from Eqs. (B4) and (B5):

$$\dot{\rho}_{12} = \frac{\gamma}{1 + \alpha^2} \left\{ -j\rho_{12} \left[ \pm \frac{\alpha}{M_s} \Lambda_p \right] - \frac{1}{2}(\rho_{11} - \rho_{22}) \left[ \mp \Lambda_p \frac{M_x - jM_y}{M_s^2 - M_z^2} \left( 1 - j \frac{\alpha M_z}{M_s} \right) \right] \right\}. \quad (\text{B12})$$

Reformulating the expression with  $\rho_{12}$ :

$$\dot{\rho}_{12} = \frac{\gamma}{1 + \alpha^2} \cdot \rho_{12} \left\{ -j \left[ \pm \Lambda_p \frac{\alpha M_s}{M_s^2 - M_z^2} \right] \pm \frac{M_z}{M_s} \left[ \Lambda_p \frac{M_s}{M_s^2 - M_z^2} \right] \right\}. \quad (\text{B13})$$

Using Eq. (4) in the main text:

$$\dot{\rho}_{12} = -(j\omega_{\text{TLS}} + \gamma_{\text{inh}})\rho_{12} + jM_z V_{12},$$

we express the TLS terms  $\omega_{\text{TLS}}$  and  $\gamma_{\text{inh}}$ :

$$\omega_{\text{TLS}} = \pm \frac{\gamma}{(1 + \alpha^2)} \left\{ \Lambda_p \frac{\alpha M_s}{M_s^2 - M_z^2} \right\},$$

$$\gamma_{\text{inh}} = \mp \frac{\gamma}{(1 + \alpha^2)} \frac{M_z}{M_s} \left\{ \Lambda_p \frac{M_s}{M_s^2 - M_z^2} \right\}.$$

### APPENDIX C: EVALUATION OF THE EFFECTIVE INDUCED FIELD

Following Ref. [11], we evaluate the effective field along  $-\hat{z}$  from the small-angle dynamics of  $M_y$  by the effect of the fieldlike torque:

$$\frac{M_y}{M_s} = \gamma \int B_{\text{eff}}^{\text{(primary torque)}} dt \approx \gamma B_{\text{eff}}^{\text{(primary torque)}} \Delta t_{\text{pulse}}, \quad (\text{C1})$$

$$B_{\text{eff}}^{\text{(primary torque)}} = \frac{M_y}{M_s} \frac{1}{\gamma \Delta t_{\text{pulse}}}. \quad (\text{C2})$$

On the other hand, we can also evaluate the effective field from the dynamics of  $M_z$  by the effect of a dampinglike torque:

$$\frac{M_z}{M_s} = 1 - e^{-\Delta t_{\text{pulse}}/\tau_\alpha} = 1 - e^{-\Delta t_{\text{pulse}}\alpha\gamma B_{\text{eff}}^{\text{(damping torque)}}}, \quad (\text{C3})$$

$$B_{\text{eff}}^{\text{(damping torque)}} = \ln \left( \frac{M_s}{M_s - M_z} \right) \frac{1}{\alpha\gamma \Delta t_{\text{pulse}}}. \quad (\text{C4})$$

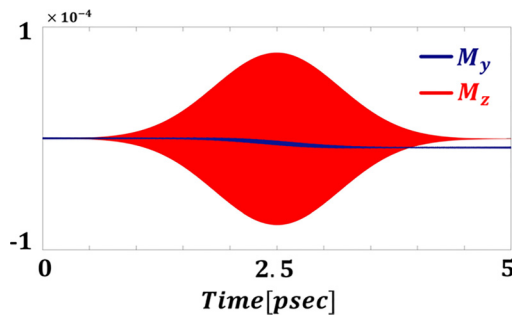


FIG. 4. Magnetization dynamics induced by a 0.3-T RCP pulse, for  $\alpha = 0.025$  and  $\tau_p = 675$  fs. Results are normalized by  $M_s$ .

For the case of Fig. 3(a) in the main text,  $B_{\text{eff}}^{\text{(damping torque)}} = 50$  mT.

In Fig. 4 we compare the action of our mechanism to that demonstrated by Choi *et al.* [11] for a 10-nm Co/4-nm Pt sample. The figure presents the optically induced dynamics of  $M_y$  and  $M_z$ . We introduce an RCP pulse to the LLG equation and set  $\Delta t_{\text{pulse}} = 1.1$  ps,  $t_{\text{peak}} = 2.5$  ps, and  $\alpha = 0.025$ . In Fig. 4 we find that introducing a CP optical field of 0.3 T in the LLG equation results in  $M_y = 8.3 \times 10^{-6}$  and  $M_z = 4.3 \times 10^{-7}$ , so that  $B_{\text{eff}}^{\text{(primary torque)}} = \frac{M_y}{M_s} \frac{1}{\gamma \Delta t_{\text{pulse}}} \sim 0.25$  mT and  $B_{\text{eff}}^{\text{(primary torque)}} = \frac{M_z}{M_s} \frac{1}{\gamma \Delta t_{\text{pulse}}} \sim 0.014$  mT.

The influence of the magnetic anisotropy on  $B_{\text{eff}}^{\text{(primary torque)}}$  was examined as well. To this end, we introduced the anisotropy field  $\vec{H}_{\text{anis}} = -M_z \hat{z}$  to the LLG equation in addition to the optical pulse simulated in Fig. 3(a) of the main text. Figure 5 readily shows that the longitudinal torque induced by the optical pulse remains unaffected by  $\vec{H}_{\text{anis}}$ . The change in  $B_{\text{eff}}^{\text{(primary torque)}}$  was found to be smaller than  $10^{-4}\%$ .

### APPENDIX D: DERIVATION OF $\Gamma/M_s$

The optically induced transition, for the case of  $\eta \geq 1$ , can be described analytically by making the following assumptions. To this end, we define  $H_{\text{peak}}$  corresponding to  $\eta = 1$  by  $H_{\text{th}} = \frac{\omega_{\text{opt}}}{2\pi\gamma\alpha}$ . We first assume that  $\vec{M}$  is already locked to  $\vec{H}_{\text{opt}}$  at  $t = t_{\text{peak}}$  and precesses in the  $x$ - $y$  plane, and that the switching is initiated when the power of the pulse reduces to half the power of electromagnetic radiation having  $|\vec{H}| = H_{\text{th}}$ . This occurs when  $\vec{H}_{\text{opt}}(t)$  reaches the magnitude of  $H_{\text{crit}} = H_{\text{th}}/\sqrt{2}$ . We calculate the transition rate,  $\Gamma$ , from  $M_z$  when the  $\hat{z}$  torque is maximal. We find this point to occur approximately when  $|M_z(t)| \sim 0.5M_s$  at which  $|\vec{H}_{\text{opt}}(t)|$  reduces to  $H_{1/2} = 0.27H_{\text{th}}$  as shown in Fig. 6.

We consider the case of  $t > t_{\text{peak}} + t_{\text{crit}}$ , where  $t_{\text{crit}} = \tau_p \sqrt{2 \ln \left( \frac{H_{\text{peak}}}{H_{\text{th}}/\sqrt{2}} \right)}$ , and start by presenting the components of  $H_{\text{opt}}(t)$ :

$$H_{\text{opt } x}(t) = H_{\text{peak}} \cos(\omega_{\text{opt}} t) e^{-(t-t_{\text{peak}})^2/2\tau_p^2},$$

$$H_{\text{opt } y}(t) = \pm H_{\text{peak}} \sin(\omega_{\text{opt}} t) e^{-(t-t_{\text{peak}})^2/2\tau_p^2},$$

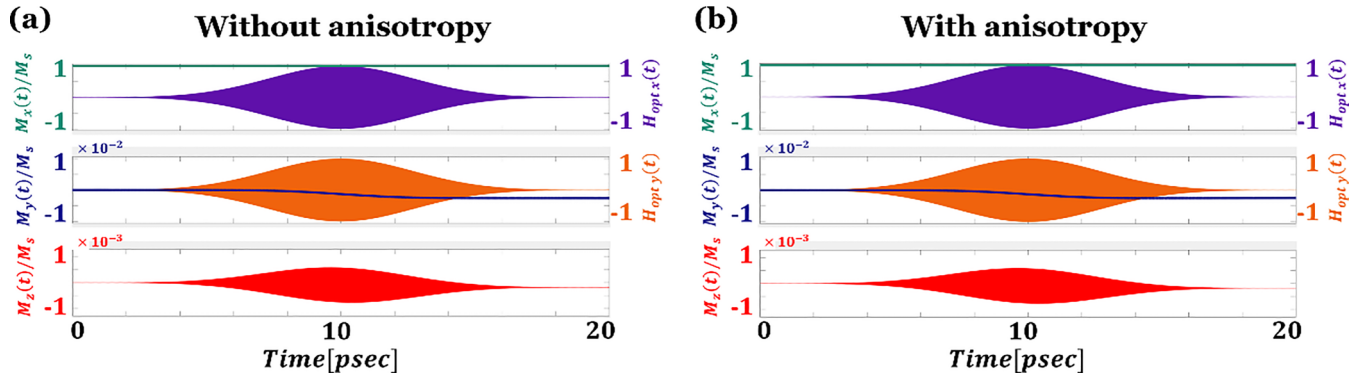


FIG. 5. Inclusion of  $\vec{H}_{\text{anis}}$ . Temporal trace of the magnetization simulated for the same conditions as in Fig. 3(a) in the main text (a) without the inclusion of anisotropy, and (b) with the inclusion of anisotropy.  $\vec{M}$  was initialized in the  $\hat{x}$  direction.

for the RCP and LCP pulses. We assume that  $H_{\text{peak}} \geq H_{\text{th}}$  and accordingly  $\vec{M}$  is locked to the optical pulse at  $t = t_{\text{peak}}$ , and starts to decay from the  $x$ - $y$  plane only after  $t = t_{\text{peak}} + t_{\text{crit}}$ . We assume that  $M_x$  and  $M_y$  have Gaussian envelopes:

$$M_x(t) = M_s \cos(\omega_{\text{opt}} t) e^{-(t-t_{\text{peak}}-t_{\text{crit}})^2/2\tau_M^2},$$

$$M_y(t) = \pm M_s \sin(\omega_{\text{opt}} t) e^{-(t-t_{\text{peak}}-t_{\text{crit}})^2/2\tau_M^2},$$

for the RCP and LCP pulses, where  $t_{\text{crit}}$  and  $\tau_M$  define their Gaussian profile.  $\tau_M$  is the relaxation rate of  $\vec{M}$  from the CP motion, which we now turn to calculate: At  $t = t_{\text{peak}} + t_{1/2}$ ,  $H_{\text{opt}}(t)$  decreases to  $H_{1/2}$  and  $|M_z(t)|$  reaches  $0.5M_s$ , so that

$$M_x^2(t = t_{\text{peak}} + t_{1/2}) + M_y^2(t = t_{\text{peak}} + t_{1/2}) = \frac{3}{4}M_s^2.$$

In this case:

$$e^{-(t_{1/2}-t_{\text{crit}})^2/\tau_M^2} = \frac{3}{4},$$

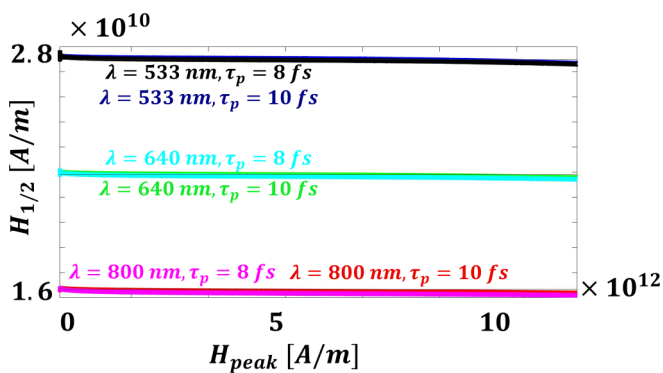


FIG. 6. Numerical calculation of  $H_{1/2}$ , the amplitude of the Gaussian envelope of  $H_{\text{opt}}(t)$  when  $|M_z(t)|$  decreases to  $0.5M_s$  during the reversal.  $H_{\text{peak}} \in [\frac{\omega_{800 \text{ nm}}(1+\alpha^2)}{2\pi\gamma\alpha}, 150 \cdot \frac{\omega_{800 \text{ nm}}(1+\alpha^2)}{2\pi\gamma\alpha}]$ , where  $\omega_{800 \text{ nm}}$  corresponds to an optical wavelength of 800 nm and  $\alpha = 0.025$ . The different curves correspond to applied pulses with three different wavelengths  $\lambda \in \{533, 640, \text{ and } 800 \text{ nm}\}$  and two different pulse durations  $\tau_p \in \{8 \text{ and } 10 \text{ fs}\}$ . The three solid thin lines correspond to  $H_{1/2}^{\text{analytical}} = 0.27 \frac{\omega_{\text{opt}}(1+\alpha^2)}{2\pi\gamma\alpha}$  for the three different wavelengths and reproduce the calculated curves well.  $H_{1/2}$  is seen to be independent from  $\tau_p$ .

which determines  $\tau_M$  by the relation

$$\begin{aligned} \tau_M &= \frac{(t_{1/2} - t_{\text{crit}})}{\sqrt{\ln\left(\frac{4}{3}\right)}} \\ &= \frac{\tau_p}{\sqrt{\ln\left(\frac{4}{3}\right)}} \left[ \sqrt{2 \ln\left(\frac{H_{\text{peak}}}{0.27H_{\text{th}}}\right)} - \sqrt{2 \ln\left(\frac{H_{\text{peak}}}{H_{\text{th}}/\sqrt{2}}\right)} \right]. \end{aligned}$$

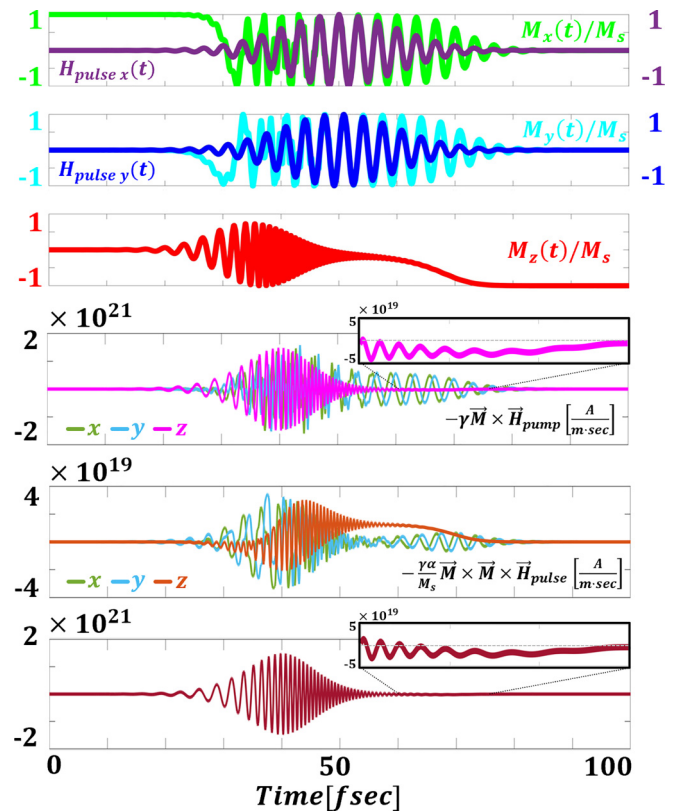


FIG. 7. First, second, and third panels depict the temporal evolution of the normalized  $M_x$  and  $H_{\text{pulse } x}$ ,  $M_y$  and  $H_{\text{pulse } y}$ , and  $M_z$ , respectively. Fourth, fifth, and sixth panels depict the temporal evolution of the not-normalized primary torque, damping torque, and  $\hat{z}$  component of the total torque, respectively. Insets:  $\hat{z}$  component of the primary (total) torque for  $t = 60$ – $75$  fs where the reversal of  $M_z$  occurs.  $\eta = 1$ ,  $\alpha = 0.035$ ,  $\tau_p = 10$  fs.



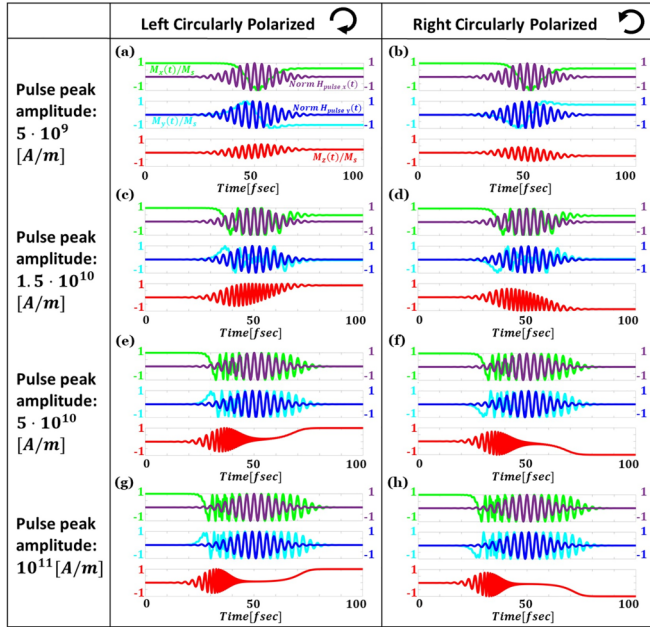


FIG. 8. Magnetization switching induced by RCP and LCP pulses, for  $\alpha = 0.025$  and  $\tau_p = 10$  fs, for a 1- $\mu\text{m}$  wavelength.

Finally, using the normalization condition of  $\vec{M}$ ,  $|\vec{M}|^2 = M_s^2$ , we find that

$$M_z(t) = \mp M_s \sqrt{1 - e^{-(t-t_{\text{peak}} - t_{\text{crit}})^2 / \tau_M^2}}.$$

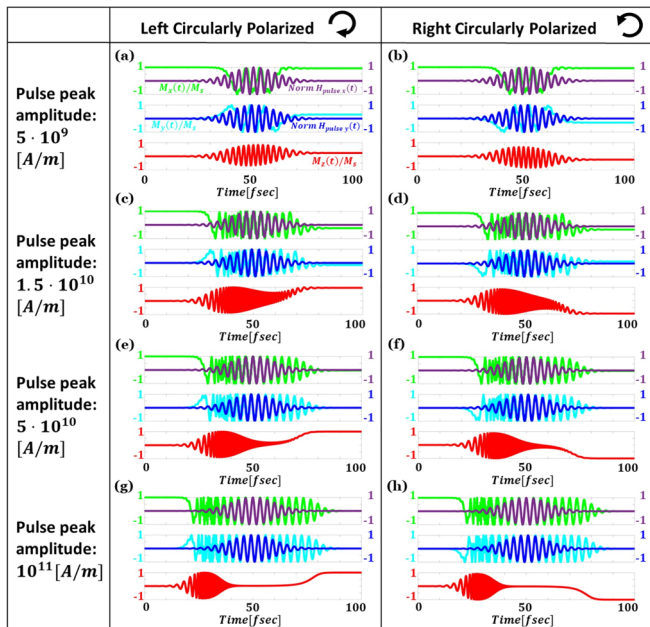


FIG. 9. Magnetization switching induced by RCP and LCP pulses, for  $\alpha = 0.0075$  and  $\tau_p = 10$  fs, for a 1- $\mu\text{m}$  wavelength.

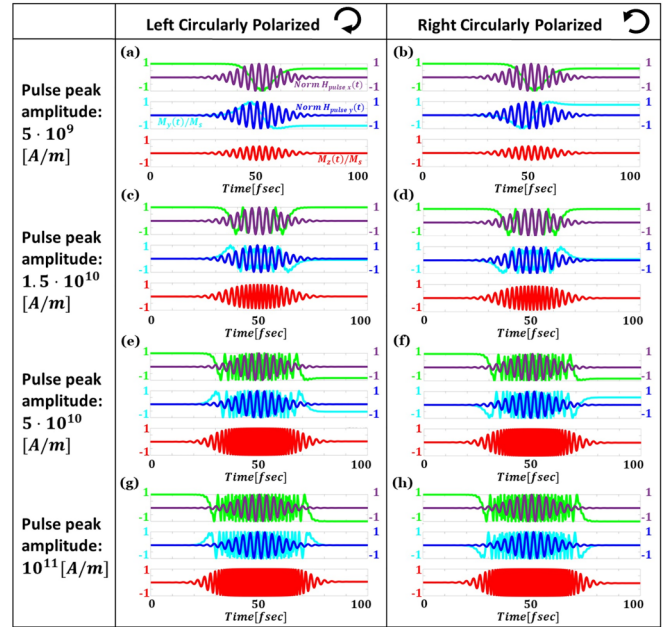


FIG. 10. Magnetization switching cannot be induced by RCP and LCP pulses when  $\alpha = 10^{-4}$  and  $\tau_p = 10$  fs, for a 1- $\mu\text{m}$  wavelength.

We calculated the transition rate,  $\Gamma$ , by taking the slope of  $M_z(t)$  at  $t = t_{\text{peak}} + t_{1/2}$ , from which we find that

$$\frac{\Gamma}{M_s} = \mp \frac{3}{2} \frac{\sqrt{\ln(\frac{4}{3})}}{\tau_M} \approx \mp \frac{0.305}{\tau_p \left[ \sqrt{\ln\left(\frac{H_{\text{peak}}}{0.27H_{\text{th}}}\right)} - \sqrt{\ln\left(\frac{H_{\text{peak}}}{\frac{H_{\text{th}}}{\sqrt{2}}}\right)} \right]}.$$

#### APPENDIX E: MAGNETIZATION REVERSAL INDUCED BY CIRCULARLY POLARIZED MAGNETIC FIELD PULSES

Figure 7 presents a similar simulation to Fig. 3(c) from the main text with additional details on the torques. Figures 8–11 present the magnetization switching induced by circularly polarized pulses, in the absence of other excitations. The figures illustrate the effect of different pulse amplitudes for LCP and RCP pulses. They clearly show that while the phase-locking condition  $H_{\text{peak}} \geq H_{\text{th}} = \frac{\omega_{\text{opt}}(1+\alpha^2)}{2\pi\gamma\alpha}$  is fulfilled, the LCP pulses fully reverse the magnetization towards  $+z$  while RCP pulses reverse it towards  $-z$ . In Fig. 8  $\alpha = 0.025$  while in Fig. 9  $\alpha = 0.0075$ . In this case, a smaller damping still results in reversal. However, since the damping is at the core of the interaction, for the case where  $\alpha = 10^{-4}$  no reversal is built from cycle to cycle for any pulse amplitude, as readily seen in Fig. 10. In Fig. 11  $\alpha = 0.025$  and the timescale is enlarged by three orders of magnitude, namely to the  $\sim 30$ -ps duration, while the wavelength is increased to 1 mm. In this case, the  $H_{\text{th}}$  amplitudes required for the full magnetization reversal are also lower by three orders of magnitude as compared to

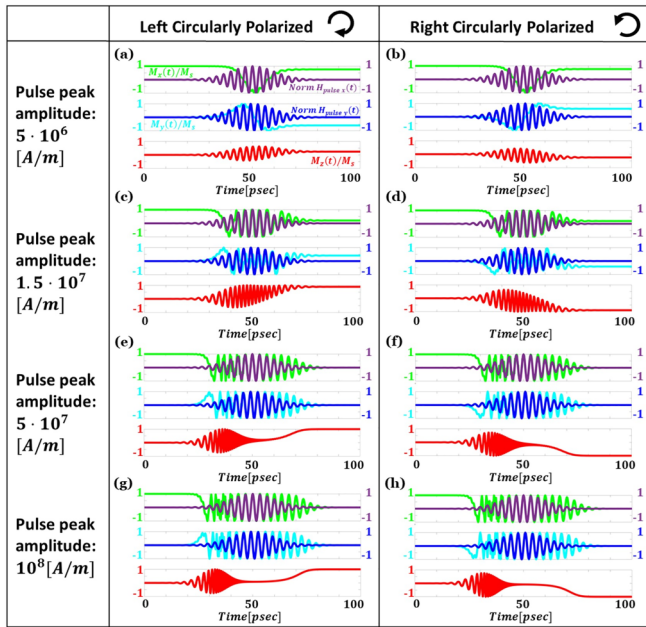


FIG. 11. Magnetization switching induced by RCP and LCP pulses, for  $\alpha = 0.025$  and  $\tau_p = 10$  ps, for a 1-mm wavelength.

the 30-fs pulses in Figs. 8–11. In Fig. 12 we show the pivotal role of  $\alpha$  to the interaction and simulate the same conditions

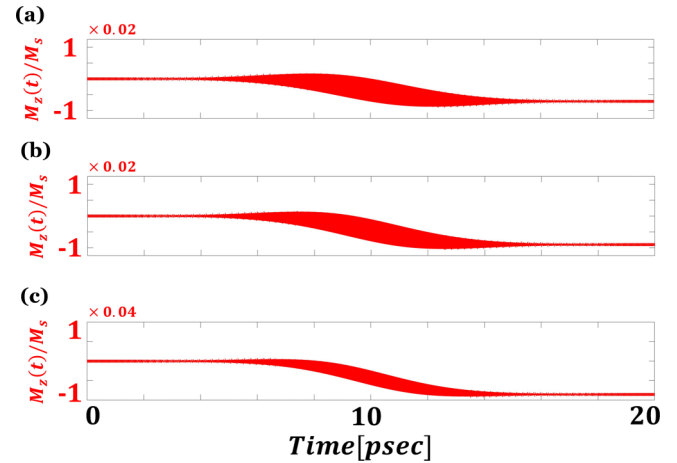


FIG. 12. Temporal trace of  $M_z/M_s$  simulated for the same conditions as in Fig. 3(a) in the main text, for  $H_{\text{peak}} = 7.3 \times 10^7$  A/m and  $\alpha = 0.025$  (a),  $\alpha = 0.035$  (b), and  $\alpha = 0.06$  (c). It is readily seen that the longitudinal torque is enhanced with  $\alpha$ .

as in Fig. 3(a) in the main text for different  $\alpha$  values and for  $H_{\text{peak}} = 7.3 \times 10^7$  A/m. It is readily seen that the response is enhanced with  $\alpha$ , namely  $\frac{M_z}{M_s} = 0.014$ , 0.02, and 0.034 for  $\alpha = 0.025$ , 0.035, and 0.06, respectively.

- [1] C. D. Stanciu, F. Hansteen, A. V. Kimel, A. Kirilyuk, A. Tsukamoto, A. Itoh, and T. Rasing, All-optical magnetic recording with circularly polarized light, *Phys. Rev. Lett.* **99**, 047601 (2007).
- [2] K. Vahaplar, A. M. Kalashnikova, A. V. Kimel, S. Gerlach, D. Hinzke, U. Nowak, R. Chantrell, A. Tsukamoto, A. Itoh, A. Kirilyuk, and T. Rasing, All-optical magnetization reversal by circularly polarized laser pulses: Experiment and multiscale modeling, *Phys. Rev. B* **85**, 104402 (2012).
- [3] A. Hassdenteufel, B. Hebler, C. Schubert, A. Liebig, M. Teich, M. Helm, M. Aeschlimann, M. Albrecht, and R. Bratschitsch, Thermally assisted all-optical helicity dependent magnetic switching in amorphous  $\text{Fe}_{100-x}\text{Tb}_x$  alloy films, *Adv. Mater.* **25**, 3122 (2013).
- [4] S. Alebrand, M. Gottwald, M. Hehn, D. Steil, M. Cinchetti, D. Lacour, E. E. Fullerton, M. Aeschlimann, and S. Mangin, Light-induced magnetization reversal of high-anisotropy TbCo alloy films, *Appl. Phys. Lett.* **101**, 162408 (2012).
- [5] S. Mangin, M. Gottwald, C. H. Lambert, D. Steil, V. Uhlř, L. Pang, M. Hehn, S. Alebrand, M. Cinchetti, G. Malinowski, Y. Fainman, M. Aeschlimann, and E. E. Fullerton, Engineered materials for all-optical helicity-dependent magnetic switching, *Nat. Mater.* **13**, 286 (2014).
- [6] C.-H. Lambert, S. Mangin, B. S. D. C. S. Varaprasad, Y. K. Takahashi, M. Hehn, M. Cinchetti, G. Malinowski, K. Hono, Y. Fainman, M. Aeschlimann, and E. E. Fullerton, All-optical control of ferromagnetic thin films and nanostructures, *Science* **345**, 1337 (2014).
- [7] D. Steil, S. Alebrand, A. Hassdenteufel, M. Cinchetti, and M. Aeschlimann, All-optical magnetization recording by tailoring optical excitation parameters, *Phys. Rev. B* **84**, 224408 (2011).
- [8] K. Vahaplar, A. M. Kalashnikova, A. V. Kimel, D. Hinzke, U. Nowak, R. Chantrell, A. Tsukamoto, A. Itoh, A. Kirilyuk, and T. Rasing, Ultrafast path for optical magnetization reversal via a strongly nonequilibrium state, *Phys. Rev. Lett.* **103**, 117201 (2009).
- [9] A. Kirilyuk, A. V. Kimel, and T. Rasing, Ultrafast optical manipulation of magnetic order, *Rev. Mod. Phys.* **82**, 2731 (2010).
- [10] G. Kichin, M. Hehn, J. Gorchon, G. Malinowski, J. Hohlfeld, and S. Mangin, From multiple- to single-pulse all-optical helicity-dependent switching in ferromagnetic Co/Pt multilayers, *Phys. Rev. Appl.* **12**, 024019 (2019).
- [11] G.-M. Choi, A. Schleife, and D. G. Cahill, Optical-helicity-driven magnetization dynamics in metallic ferromagnets, *Nat. Commun.* **8**, 15085 (2017).
- [12] P. Němec, E. Rozkotová, N. Tesařová, F. Trojánek, E. De Ranieri, K. Olejník, J. Zemen, V. Novák, M. Cukr, P. Malý, and T. Jungwirth, Experimental observation of the optical spin transfer torque, *Nat. Phys.* **8**, 411 (2012).
- [13] F. Freimuth, S. Blügel, and Y. Mokrousov, Laser-induced torques in metallic ferromagnets, *Phys. Rev. B* **94**, 144432 (2016).
- [14] G. P. Zhang, T. Latta, Z. Babyak, Y. H. Bai, and T. F. George, All-optical spin switching: A new frontier in femtomagnetism—A short review and a simple theory, *Mod. Phys. Lett. B* **30**, 16300052 (2016).

- [15] P. Zhang, T.-F. Chung, Q. Li, S. Wang, Q. Wang, W. L. B. Huey, S. Yang, J. E. Goldberger, J. Yao, and X. Zhang, All-optical switching of magnetization in atomically thin CrI<sub>3</sub>, *Nat. Mater.* **21**, 1373 (2022).
- [16] N. Yoshikawa, K. Ogawa, Y. Hirai, K. Fujiwara, J. Ikeda, A. Tsukazaki, and R. Shimano, Non-volatile chirality switching by all-optical magnetization reversal in ferromagnetic Weyl semimetal Co<sub>3</sub>Sn<sub>2</sub>S<sub>2</sub>, *Commun. Phys.* **5**, 328 (2022).
- [17] E. Beaurepaire, J. C. Merle, A. Daunois, and J. Y. Bigot, Ultrafast spin dynamics in ferromagnetic nickel, *Phys. Rev. Lett.* **76**, 4250 (1996).
- [18] S. Alebrand, A. Hassdenteufel, D. Steil, M. Cinchetti, and M. Aeschlimann, Interplay of heating and helicity in all-optical magnetization switching, *Phys. Rev. B* **85**, 092401 (2012).
- [19] R. Chimata, L. Isaeva, K. Kádas, A. Bergman, B. Sanyal, J. H. Mentink, M. I. Katsnelson, T. Rasing, A. Kirilyuk, A. Kimel, O. Eriksson, and M. Pereiro, All-thermal switching of amorphous Gd-Fe alloys: Analysis of structural properties and magnetization dynamics, *Phys. Rev. B* **92**, 094411 (2015).
- [20] L. Avilés-Félix, L. Farcis, Z. Jin, L. Álvaro-Gómez, G. Li, K. T. Yamada, A. Kirilyuk, A. V. Kimel, T. Rasing, B. Dieny, R. C. Sousa, I. L. Prejbeanu, and L. D. Buda-Prejbeanu, All-optical spin switching probability in [Tb/Co] multilayers, *Sci. Rep.* **11**, 6576 (2021).
- [21] J. Gorchon, Y. Yang, and J. Bokor, Model for multishot all-thermal all-optical switching in ferromagnets, *Phys. Rev. B* **94**, 020409(R) (2016).
- [22] A. R. Khorsand, M. Savoini, A. Kirilyuk, A. V. Kimel, A. Tsukamoto, A. Itoh, and T. Rasing, Role of magnetic circular dichroism in all-optical magnetic recording, *Phys. Rev. Lett.* **108**, 127205 (2012).
- [23] Y. Quessab, M. Deb, J. Gorchon, M. Hehn, G. Malinowski, and S. Mangin, Resolving the role of magnetic circular dichroism in multishot helicity-dependent all-optical switching, *Phys. Rev. B* **100**, 024425 (2019).
- [24] F. Hansteen, A. Kimel, A. Kirilyuk, and T. Rasing, Nonthermal ultrafast optical control of the magnetization in garnet films, *Phys. Rev. B* **73**, 014421 (2006).
- [25] M. S. El Hadri, P. Pirro, C. H. Lambert, S. Petit-Watelot, Y. Quessab, M. Hehn, F. Montaigne, G. Malinowski, and S. Mangin, Two types of all-optical magnetization switching mechanisms using femtosecond laser pulses, *Phys. Rev. B* **94**, 064412 (2016).
- [26] T. A. Ostler, J. Barker, R. F. L. Evans, R. W. Chantrell, U. Atxitia, O. Chubykalo-Fesenko, S. El Moussaoui, L. Le Guyader, E. Mengotti, L. J. Heyderman, F. Nolting, A. Tsukamoto, A. Itoh, D. Afanasiev, B. A. Ivanov, A. M. Kalashnikova, K. Vahaplar, J. Mentink, A. Kirilyuk, T. Rasing, and A. V. Kimel, Ultrafast heating as a sufficient stimulus for magnetization reversal in a ferrimagnet, *Nat. Commun.* **3**, 666 (2012).
- [27] J. Yao, G. P. Agrawal, P. Gallion, and C. M. Bowden, Semiconductor laser dynamics beyond the rate-equation approximation, *Opt. Commun.* **119**, 246 (1995).
- [28] A. Capua, O. Karni, and G. Eisenstein, A finite-difference time-domain model for quantum-dot lasers and amplifiers in the Maxwell and Schrödinger framework, *IEEE J. Sel. Top. Quantum Electron.* **19**, 1 (2013).
- [29] A. Capua, O. Karni, G. Eisenstein, V. Sichkovskiy, V. Ivanov, and J. P. Reithmaier, Coherent control in a semiconductor optical amplifier operating at room temperature, *Nat. Commun.* **5**, 5025 (2014).
- [30] R. P. Feynman, F. L. Vernon, and R. W. Hellwarth, Geometrical representation of the Schrödinger equation for solving maser problems, *J. Appl. Phys.* **28**, 49 (1957).
- [31] G. Klughertz, L. Friedland, P.-A. Hervieux, and G. Manfredi, Autoresonant switching of the magnetization in single-domain nanoparticles: Two-level theory, *Phys. Rev. B* **91**, 104433 (2015).
- [32] G. Klughertz, L. Friedland, P.-A. Hervieux, and G. Manfredi, Spin-torque switching and control using chirped AC currents, *J. Phys. D: Appl. Phys.* **50**, 415002 (2017).
- [33] M. Brik, N. Bernstein, and A. Capua, Coherent control in ferromagnets driven by microwave radiation and spin polarized current, *Phys. Rev. B* **102**, 224308 (2020).
- [34] B. Assouline, M. Brik, N. Bernstein, and A. Capua, Amplification of electron-mediated spin currents by stimulated spin pumping, *Phys. Rev. Res.* **4**, L042014 (2022).
- [35] A. G. Gurevich and G. A. Melkov, *Magnetization Oscillations and Waves* (CRC Press, Boca Raton, FL, 1996).
- [36] M. Sargent, M. Scully, and W. Lamb, *Laser Physics* (CRC Press, Boca Raton, FL, 1974).
- [37] J. H. E. L. Allen, Optical resonance and two level atoms, *Phys. Bull.* **26**, 545 (1975).
- [38] A. Capua, C. Rettner, S.-H. Yang, T. Phung, and S. S. P. Parkin, Ensemble-averaged Rabi oscillations in a ferromagnetic CoFeB film, *Nat. Commun.* **8**, 16004 (2017).
- [39] N. Fujita, N. Inaba, F. Kirino, S. Igarashi, K. Koike, and H. Kato, Damping constant of Co/Pt multilayer thin-film media, *J. Magn. Magn. Mater.* **320**, 3019 (2008).
- [40] A. H. Morrish, *The Physical Principles of Magnetism* (Wiley-IEEE Press, New York, NY, 2001).
- [41] A. Capua, S.-H. Yang, T. Phung, and S. S. P. Parkin, Determination of intrinsic damping of perpendicularly magnetized ultrathin films from time-resolved precessional magnetization measurements, *Phys. Rev. B* **92**, 224402 (2015).
- [42] Y. Tserkovnyak, A. Brataas, and G. E. W. Bauer, Enhanced Gilbert damping in thin ferromagnetic films, *Phys. Rev. Lett.* **88**, 117601 (2002).
- [43] M. Caminale, A. Ghosh, S. Auffret, U. Ebels, K. Ollefs, F. Wilhelm, A. Rogalev, and W. E. Bailey, Spin pumping damping and magnetic proximity effect in Pd and Pt spin-sink layers, *Phys. Rev. B* **94**, 014414 (2016).
- [44] R. Mondal, M. Berritta, C. Paillard, S. Singh, B. Dkhil, P. M. Oppeneer, and L. Bellaïche, Relativistic interaction Hamiltonian coupling the angular momentum of light and the electron spin, *Phys. Rev. B* **92**, 100402(R) (2015).
- [45] M. Berritta, R. Mondal, K. Carva, and P. M. Oppeneer, *Ab initio* theory of coherent laser-induced magnetization in metals, *Phys. Rev. Lett.* **117**, 137203 (2016).
- [46] A. Qaiumzadeh and M. Titov, Theory of light-induced effective magnetic field in Rashba ferromagnets, *Phys. Rev. B* **94**, 014425 (2016).
- [47] A. Capua, T. Wang, S.-H. Yang, C. Rettner, T. Phung, and S. S. P. Parkin, Phase-resolved detection of the spin Hall angle by optical ferromagnetic resonance in perpendicularly magnetized thin films, *Phys. Rev. B* **95**, 064401 (2017).
- [48] T. Devolder, S. Couet, J. Swerts, and G. S. Kar, Gilbert damping of high anisotropy Co/Pt multilayers, *J. Phys. D Appl. Phys.* **51**, 135002 (2018).